LIMNOLOGY and OCEANOGRAPHY

ASLO

*Limnol. Oceanogr.* 65, 2020, 1818–1833

doi: 10.1002/lno.11420

# Flow and diffusion around and within diatom aggregates: Effects of aggregate composition and shape

**Eva-Maria Zetsche**,[1,2,3*,a] **Ann I. Larsson**,[4] **Morten H. Iversen**,[5,6] **Helle Ploug**[1]

[1]Department of Marine Sciences, University of Gothenburg, Box 461, 40530 Gothenburg, Sweden
[2]Analytical, Environmental and Geo-Chemistry, Vrije Universiteit Brussel (VUB), Pleinlaan 2, B-1050 Brussels, Belgium
[3]Royal Netherlands Institute for Sea Research, PO Box 140, 4400 AC Yerseke, The Netherlands
[4]Department of Marine Sciences, Tjärnö Marine Laboratory, University of Gothenburg, Strömstad, Sweden
[5]Helmholtz Young Investigator Group SEAPUMP, Alfred Wegener Institute for Polar and Marine Research, Bremerhaven, Germany
[6]MARUM, Center for Marine Environmental Sciences, University of Bremen, Bremen, Germany

## *Abstract*

Diatom aggregates constitute a significant fraction of the particle flux from the euphotic zone into the mesopelagic ocean as part of the ocean's biological carbon pump. Modeling studies of their exchange processes with the surrounding water usually assume spherical shape and that aggregates are impermeable to flow. Using particle image velocimetry, we examined flow distributions around individual aggregates of various irregular shapes formed from two different diatom species: (1) *Skeletonema marinoi*, known for its cell–cell stickiness, and (2) *Chaetoceros affinis*, exhibiting cell-TEP (transparent exopolymeric particles) stickiness. *Chaetoceros* aggregates formed porous, highly irregularly shaped aggregates as compared to the more compact and near-spherical *Skeletonema* aggregates, yet flow distributions around both types of aggregates were relatively similar at a millimeter scale. At a micrometer scale, the irregular shape of diatom aggregates caused velocity gradients and vorticity close to the surface to locally vary more than for spherical model aggregates (agar-yeast spheres). Water was deflected from the surface of all aggregate types and we found no direct evidence that flow occurred within aggregates. Digital holographic imaging and Alcian blue staining revealed a substantial presence of TEP likely clogging the interstitial pore spaces in *Chaetoceros* aggregates. Radial oxygen concentration distributions measured by $O_2$ microsensors within the aggregates were similar to those modeled for aggregates and spheres impermeable to flow. Thus, transport of gases, nutrients, and solutes likely occurs by diffusion, even within large, irregularly shaped diatom aggregates during sinking.

Diatoms are one of the most abundant types of phytoplankton and contribute approximately 20% of the earth's primary production (Nelson et al. 1995). Diatoms often follow a bloom-and-bust cycle with blooms terminated by the formation of fast-sinking aggregates (>0.5 mm) (Alldredge and Gotschalk 1988). They constitute a significant fraction of the particle flux from the euphotic zone into the mesopelagic ocean as part of the "biological carbon pump" (Volk and Hoffert 1985; Turner 2015). This particle export from the upper ocean to greater depths and the seafloor not only redistributes carbon and nutrients in the ocean, but plays a major role in the uptake of atmospheric carbon dioxide ($CO_2$) by the ocean (Volk and Hoffert 1985; Bergkvist et al. 2018). The vertical carbon flux attenuates greatly in the ocean's twilight zone and the fate of carbon in sinking aggregates is an ongoing research topic (Sanders et al. 2016; Siegel et al. 2016).

Aggregates sinking through the water column scavenge other particles and are at the same time remineralized by colonizing bacteria and protozoa (Simon et al. (2002) and references therein); they function as "hotspots" of microbially driven remineralization (Grossart and Ploug 2001; Grossart et al. 2007; Bižić-Ionescu et al. 2018). Aggregate-associated bacteria are often present in concentrations two to three orders of magnitude higher than that in the ambient water (Simon et al. 2002; Thiele et al. 2015) and appear to function fundamentally differently to the communities living in the ambient seawater (Delong et al. 1993; Moeseneder et al. 2001; Thiele et al. 2015). Microbes in aggregates solubilize and remineralize particulate organic

*Correspondence: eva-maria.zetsche@uantwerpen.be



[a]Present address: Department of Biology, University of Antwerp, Universiteitsplein 1, 2610 Wilrijk, Belgium

matter (POM) releasing carbon dioxide as well as dissolved organic matter (DOM) and nutrients (Smith et al. 1992; Ploug and Bergkvist 2015; Bergkvist et al. 2018). Total carbon turnover in sinking aggregates is dependent on the influx and efflux of oxygen, nutrients, and DOM to and from the aggregate as determined by flow, reaction rate, and molecular diffusion as well as aggregate properties such as porosity, composition and presence of transparent exopolymeric particles (TEP), among others (Moradi et al. 2018). Under $O_2$ saturation in the ambient water, efficient mass transfer by diffusion across the aggregate-water interface has been demonstrated using $O_2$ microsensors (Smith et al. 1992; Ploug et al. 1997; Ploug and Jørgensen 1999; Ploug et al. 1999*a*). In oxygen minimum zones, however, $O_2$ respiration within aggregates potentially becomes diffusion limited, and diatom aggregates can be microenvironments hosting various anaerobic N-transformation processes (Ploug 2001; Ploug and Bergkvist 2015; Stief et al. 2016).

Diatom aggregates have been extensively studied over the past decades with regard to a wide range of biological, chemical, and physical studies (e.g., Burd and Jackson 2009; Turner 2015). They are well known to be highly porous with porosities >99.9% (Alldredge and Gotschalk 1988; Iversen and Ploug 2010), where porosity defines the fraction of volume that is not diatom cells. A high porosity, however, does not necessarily imply a high permeability as pore spaces may in fact be occupied by TEP or are too small to admit flow through the aggregate interior (Ploug and Passow 2007). The volume fraction of TEP in diatom aggregates can be >90%. Consequently, TEP can affect aggregate hydrodynamics in such a way that aggregates containing high amounts of TEP may, in fact, behave like spheres impermeable to flow (Ploug and Passow 2007).

Model studies of mass transfer to and from sinking aggregates furthermore assume a spherical geometry of aggregates (Logan and Alldredge 1989; Kiørboe et al. 2001; Moradi et al. 2018). Many diatom aggregates, however, show irregular geometry (Alldredge and Gotschalk 1988). Few empirical investigations of the flow distribution around sinking diatom aggregates with irregular shapes have been reported (Ploug and Jørgensen 1999). This study investigated how flow distributions are affected by shape irregularities but also by the presence of TEP. We used particle image velocimetry (PIV) combined with a vertical flow system to measure flow fields around two different types of diatom aggregates: (1) dense, compact aggregates formed from the species *Skeletonema marinoi* and (2) large, flocculent aggregates formed from the species *Chaetoceros affinis*, as well as around (3) agar spheres as reference aggregates. Aggregate characteristics, including radial oxygen concentration distributions and the presence of TEP using holographic imaging and Alcian blue staining were determined for all diatom aggregates. PIV was used to study the flow distributions around sinking marine aggregates at high spatial resolution.

## Materials and methods

Diatom and model aggregates were produced in the laboratory and studied in a vertical flow chamber (Fig. 1) described in full detail in Ploug and Jørgensen (1999). In brief, the flow chamber was a 10 cm high plexiglass tube (5 cm diameter) with a net extended in the middle. Fluid flow was supplied from below and a disperser was positioned at the inlet to the lower chamber below the net. The net created a laminar flow that was relatively uniform across the upper chamber from 1 mm above the net at flow velocities >1.0 mm $s^{-1}$ as documented by PIV in Ploug and Jørgensen (1999). The chamber was positioned in an aquarium filled with the same water as that used for the roller-tank incubations (0.2 $\mu$m filtered seawater at 17°C with a salinity of 31). The aquarium water was maintained at a constant temperature of 17°C using a Julabo F12-ED Refrigerated/Heating Circulator (Germany). The flow chamber was used in combination with PIV. We characterized aggregates with respect to size, sinking velocity, dry weight, TEP content, and radial oxygen distribution. The experiment was carried out in a thermostated room at 17°C.

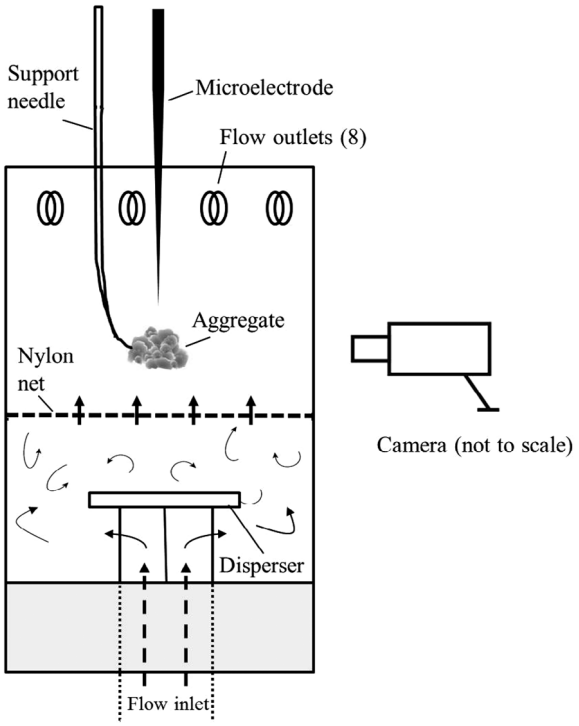


**Fig. 1** Setup of a vertical flow chamber depicting the approximate positioning of the profiling microelectrode used for measuring oxygen concentrations, the needle occasionally used for stabilization during particle image velocimetry (PIV) measurements as well as the position of an aggregate approximately one diameter above the net. The PIV laser sheet is projected into the chamber from behind the flow chamber centered on the aggregate, and the PIV camera is facing the laser sheet from the right-hand side (modified from Ploug and Jørgensen (1999)).

### Diatom aggregates

Two cultures were used: (1) *S. marinoi* (North Sea) and (2) *C. affinis* (North Sea), and are hereafter referred to as *Skeletonema* and *Chaetoceros*, respectively. Both cultures were grown at 16°C in 0.2 $\mu$m filtered seawater (salinity of 31) enriched with nutrients according to f/2 medium (Guillard 1975). The f/2 medium used for the diatoms was enriched with silicate at a molar ratio of nitrate to silicate of 2.9. The cultures were kept under a light:dark cycle (12:12 h) until they were harvested and incubated in 1.4 L Plexiglas cylinders (roller tanks) to form aggregates (Shanks and Edmondson 1989). Roller tank incubations were carried out in order to obtain aggregates formed with *Skeletonema* and *Chaetoceros* at a cell concentration of $9 \times 10^6$ cells $L^{-1}$ and at two higher cell concentrations of approx. $20 \times 10^6$ and $30 \times 10^6$ cells $L^{-1}$. The roller tanks were rotated on a rolling table at 1.5 rpm in the dark at 17°C.

### Model aggregates

Model agar-yeast aggregates were made according to Cronenberg (1994). In brief, a suspension of baker's yeast in 2% (w/w) agar was made in seawater and left to cool to 40°C, before it was dripped into a beaker filled with seawater and a thin layer of paraffin oil using a glass Pasteur pipette. Each drop formed an almost perfect agar-yeast sphere within the paraffin oil layer before settling into the sea water. Spheres were subsequently rinsed and stored for up to a few days in seawater. These nearly spherical, oxygen-consuming agar-yeast aggregates with diameters between 2 and 6 mm are impermeable to flow due to their small pore sizes in the range of 100–200 nm as known for such agarose gels (Narayanan et al. 2006). Thus, these agar-yeast aggregates were used as references of spheres impermeable to flow. During PIV measurements, they were fixed in the flow chamber by a thin glass needle (< 0.5 mm width). Different Reynolds numbers were achieved by changing the flow rate through the vertical flow chamber.

### Aggregate measurements

#### *Size measurements*

Agar-yeast spheres with various diameters, and diatom aggregates with spherical to ellipsoid shapes with various sizes and surface topographies were selected for measurements. Aggregate size was measured as equivalent spherical diameter (ESD). For this, maximum lengths of two perpendicular axes of each aggregate were extracted from images of the PIV recording (see later). Aggregate volume was calculated by assuming an ellipsoid shape (V = 4/3πabc) with the two measured axes (a,b) and the average of both for the third axis (c), which was then used to calculate ESD = $2(V/[4/3\pi])^{1/3}$.

#### *Sinking velocity*

The sinking velocity of single aggregates was measured in the vertical flow system (Fig. 1). Individual aggregates were gently transferred from the roller tanks to the chamber using a wide-bore pipette. Flow was adjusted using a needle valve until the aggregate remained suspended at the point where the sinking velocity of the aggregate was balanced by the upward-directed seawater flow velocity, approximately one aggregate diameter above the net of the flow chamber (Ploug et al. 2010). This was well beyond the distance from the net where micro-jets and micro-wakes occur (0–0.5 mm) and the PIV recordings are not influenced by the presence of the net as previously shown (Ploug and Jørgensen 1999; Kiørboe et al. 2001). The sinking velocity of an aggregate was calculated by dividing the volumetric flow rate by the cross-sectional area of the chamber (Ploug et al. 2010). Triplicate measurements were made for each aggregate.

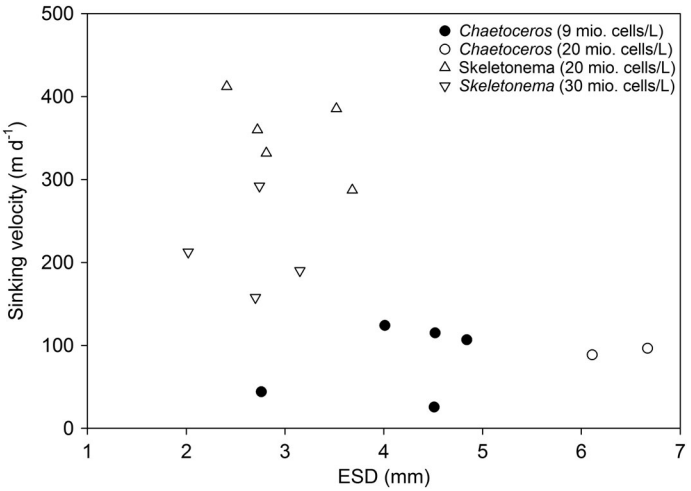


**Fig. 2** Measured sinking velocities as a function of equivalent spherical diameter (ESD) for aggregates formed at different cell concentrations of *Skeletonema marinoi* and *Chaetoceros affinis*.

#### *Aggregate dry weight*

The aggregate dry weight *DW* was determined by filtering individual diatom aggregates with known volumes onto preweighed 0.2 $\mu$m polycarbonate filters. Each filter contained one aggregate, which was gently washed with deionized water to remove any salt, dried at 50°C for 24 h and left to cool in a desiccator for 3 h before weighing on a Sartorius scale manufactured to ISO9001 standards with a sensitivity of 0.1 $\mu$g. All dry weights were made as triplicate measurements of each filter, both empty and with aggregates on.

#### *Excess density of aggregates*

Apparent excess density ($\Delta\rho$) of the aggregates was calculated using the Navier–Stokes drag equation:

$$\Delta\rho = \frac{C_D \rho_f U^2}{\frac{4}{3} g \mathrm{ESD}} \quad (1)$$

where $C_D$ is the dimensionless drag force defined in Eq. (2), $\rho_f$ is the density of sea water (1.0225 g $cm^{-3}$, at 17°C and salinity 31), $U$ is the measured sinking velocity in cm $s^{-1}$, $g$ is the

gravitational acceleration of 981 cm $s^{-2}$, and ESD the equivalent spherical diameter in cm. $C_D$ was calculated using the drag equation for Reynolds numbers (*Re)* given by White (2006):

$$C_D = \frac{24}{Re} + \frac{6}{1 + Re^{1/2}} + 0.4 \qquad 0 < Re \leq 2 \times 10^5 \tag{2}$$

where *Re* was defined as:

$$Re = \frac{Ud}{\nu} \tag{3}$$

where $d$ was the aggregate diameter and $\nu$ the kinematic viscosity of seawater ($1.1281 \times 10^{-2}$ $cm^2$ $s^{-1}$ at 17°C and salinity 31). *Re* expresses the relative importance of inertial and viscous forces acting in the vicinity of a sinking particle, in this case our aggregates.

***Solid matter density and cellular volume fraction of aggregates***

The solid matter density, $\rho_s$, was calculated from the excess density ($\Delta\rho$), the dry mass (*DW)* and volume (*V)* of individual aggregates (Alldredge and Gotschalk 1988):

$$\Delta\rho = \frac{DW}{V} \times \left(1 - \frac{\rho_f}{\rho_s}\right) \tag{4}$$

The cellular volume fraction of aggregates was subsequently calculated according to Alldredge and Gotschalk (1988):

$$cellular\ volume\ fraction = \frac{DW/\rho_s}{V} \tag{5}$$

**Velocity field measurements**

Flow around the diatom and model aggregates suspended in the vertical flow chamber was studied using PIV, a technique enabling detailed spatial information to investigate the laminar flow around sinking aggregates. When aggregates were stable in their natural suspended state at least one diameter above the net within the chamber, they were sustained in their position with a thin glass needle (<0.5 mm diameter; Fig. 1) from the back to ensure stability during the PIV measurements, particularly with respect to the fragile *Chaetoceros* aggregates. Such support needles have been used in previous studies and do not produce measurable interference with the flow and diffusion fields around aggregates as compared to theoretical distributions of flow and concentrations gradients (Kiørboe et al. 2001; Ploug et al. 2002). The water was seeded with 4 $\mu$m nylon particles (TSI Incorporated, USA) and the flow chamber was illuminated from the side with a 1 mm thick laser light sheet (continuous red light diode laser, Coherent F-system, 10 W). The laser light sheet illuminated the center of each aggregate, and an area of 27 × 20 mm around the aggregate was studied. The aggregates shaded the area opposite to the laser light source and for dense particles flow around the aggregate could only fully be studied at the illuminated side. The 1600 × 1200 pixel PIV camera (Imager PRO X, LaVision) with a 50-mm Nikkor lens was placed in front of the flow chamber and recorded 1000 images per aggregate in the single frame mode at 20 Hz. Images were analyzed with the DaVis 8.2.0 software (LaVision) using time-series cross correlation and the multipass option with a final interrogation window size of 24 × 24, or, where possible, 16 × 16 pixels for higher resolution. An overlap of 50% between interrogation windows resulted in a resolution of 5–7 flow vectors $mm^{-1}$ depending on the final interrogation window size. From the resulting instantaneous vector fields, average flow fields were produced from which velocity profiles upstream, downstream, and at the equator of each aggregate were extracted in triplicate. Off-the-equator parallel profiles were extracted perpendicular to the flow direction, while for up- and downstream profiles streamlines were followed from the pole regions in their respective directions. This allowed us to accommodate any deviations from perfectly vertical flow especially in the downstream region. The effect of aggregate shape on velocity gradients around the aggregates was further examined using the operation *extract scalar field: strain* in DaVis 8.2.0. For each interrogation window the horizontal shear rate ($dV_x/dy$) and the vertical shear rate ($dV_y/dx$) was calculated, where $V$ is the flow velocity in the horizontal ($x$) and vertical ($y$) direction, respectively. The total resultant shear rate along the surface of the aggregates was then approximated by taking the square root of the sum of squared shear. Furthermore, the vorticity fields around aggregates were calculated using the operation *extract scalar field: rotation and shear (vorticity-z)* in DaVis 8.2.0.

***Oxygen measurements***

Oxygen gradients at the aggregate-water interface and within the aggregates were measured using a Clark-type oxygen microelectrode with a tip diameter < 10 $\mu$m (Revsbech 1989) mounted in a micromanipulator and calibrated at air saturation and under anoxic conditions (Unisense, Denmark). The electrode current was measured on a picoamperemeter (Unisense, PA2000) and read on a strip chart recorder (Kipp and Zonen) at high resolution (2 $\mu$M $O_2$ $cm^{-1}$). The 90% response time of the electrode was <1 s, and the stirring sensitivity < 0.3%. During $O_2$-measurements, aggregates were either freely suspended above the net in the vertical flow chamber or fixed with a thin glass needle during measurements. Fluid motion and solute distribution in the vicinity of the aggregates under these experimental conditions are equivalent to those in the vicinity of an aggregate sinking through the water column at a velocity equal to the water flow velocity (Kiørboe et al. 2001; Moradi et al. 2018). All measurements were done at steady state of the oxygen gradients. Oxygen distributions around and within aggregates were analyzed relative to those

predicted for aggregates impermeable to flow using an analytical diffusion–reaction model (Ploug et al. 1997). In this model, the theoretical $O_2$ distribution within a sphere is calculated as a function of aggregate size, apparent diffusivity, diffusive boundary layer thickness, and $O_2$ respiration rate. For the measured aggregate size, and the diffusive boundary layer thickness, the $O_2$ respiration rate can be modeled using an Excel fitting routine of measured $O_2$ concentration distribution, and a measured or assumed apparent diffusivity within aggregates. In the present study, we assumed an apparent diffusivity of $O_2$ within aggregates of $1.73 \times 10^{-5}$ $cm^2$ $s^{-1}$ at a salinity of 30 and 17°C as measured previously in diatom aggregates (Broecker and Peng 1974; Ploug and Passow 2007). This model shows similar $O_2$ distributions in aggregates impermeable to flow as compared to those simulated by a more advanced numerical model (Moradi et al. 2018).

## Imaging of aggregates

### *Holographic imaging*

A differential digital holographic microscope (oLine $D^3$HM, Ovizio Imaging Systems NV/SA, Belgium) was used to visualize diatom aggregate structure. Details of the instrument and its imaging capability are provided in Zetsche et al. (2014, 2016*b*). A 4× Olympus objective was used as well as a 40× Leica objective for closer observations. Aggregates were gently placed into a custom-made glass-bottom dish (5 cm × 5 cm with a well depth of 5 mm) that did not alter the structure of the aggregates while they were imaged. Holograms record both the intensity information as well as phase information when the microscope's light beam (red LED light source [630 nm]) is passing through the objects of interest (e.g., aggregates, diatom cells, etc.). Differences in the phase of the transmitted light are generated by refractive index changes between the object and the surrounding medium and thus reveals differences in optical path length (OPL), therefore allowing the visualization even of apparently "transparent" substances such as exopolymers and their quantification.

### *Alcian blue staining*

Diatom aggregates were gently placed onto 0.4 $\mu$m polycarbonate filters on a filter stand, rinsed with Milli-Q water and stained with a 0.02% Alcian blue solution in 0.06% acetic acid to detect the presence of TEP (Engel 2009). Staining took ~5 s before aggregates were rinsed twice gently with Milli-Q water. Filters were then placed on a drop of immersion oil on Cytoclear slides (Sterlitech Corporation, USA), another drop of oil was added and a coverslip placed on top of the filter (Logan et al. 1994). Filters were imaged with an Olympus light microscope (BX-51) at various magnifications (4×, 10×, and 100× with oil immersion) and images captured with an attached Canon EOS 600D camera.

**Table 1.** Cell concentrations (in cells $L^{-1}$) used in the roller tanks to form aggregates are given, along with size (in equivalent spherical diameter (ESD)), dry weight (DW), dry weight per aggregate volume as well as calculated cellular volume fraction, apparent excess density, solid matter density, Reynolds (*Re*) number, the drag coefficient ($C_D$) and sinking velocity of the aggregates formed from *Skeletonema marinoi* and *Chaetoceros affinis*.

| Aggregate type and ID | Cell concentration (× $10^6$ cells $L^{-1}$) | ESD (mm) | DW ($\mu$g) | DW $vol^{-1}$ (in $\mu g\ mm^{-3}$) | Cellular volume fraction | Apparent excess density (g $cm^{-3}$) | Solid matter density (g $cm^{-3}$) | *Re* | $C_D$ | Sinking velocity (m $d^{-1}$) |
|---|---|---|---|---|---|---|---|---|---|---|
| *Chaetoceros* | | | | | | | | | | |
| *Ch1* | 9 | 4.5 | 87.2 | 1.8 | 0.002 | $3.72 \times 10^{-5}$ | 1.0415 | 1.2 | 22.9 | 25.5 |
| *Ch2* | 9 | 4.5 | 152.7 | 3.1 | 0.003 | $2.15 \times 10^{-4}$ | 1.0948 | 5.5 | 6.5 | 114.9 |
| *Ch3* | 9 | 4.8 | 879.4 | 14.8 | 0.014 | $1.74 \times 10^{-4}$ | 1.0323 | 5.6 | 6.6 | 106.7 |
| *Ch4* | 9 | 4.0 | 224.9 | 6.6 | 0.006 | $2.91 \times 10^{-4}$ | 1.0670 | 5.2 | 6.8 | 124.0 |
| *Ch5* | 9 | 2.8 | 490.3 | 44.7 | 0.044 | $1.72 \times 10^{-4}$ | 1.0241 | 1.2 | 21.9 | 43.9 |
| *Ch6* | 20 | 6.7 | 93.4 | 0.6 | 0.001 | $8.73 \times 10^{-5}$ | 1.1936 | 6.9 | 5.6 | 96.3 |
| *Ch7* | 20 | 6.1 | 218 | 1.8 | 0.002 | $9.15 \times 10^{-5}$ | 1.0741 | 5.9 | 6.3 | 88.6 |
| *Skeletonema* | | | | | | | | | | |
| *Sk1* | 30 | 3.2 | 439.1 | 26.7 | 0.025 | $7.57 \times 10^{-4}$ | 1.0499 | 6.2 | 5.9 | 190.1 |
| *Sk2* | 30 | 2.7 | 56.9 | 5.3 | 0.004 | $1.67 \times 10^{-3}$ | 1.4892 | 8.2 | 4.8 | 292.0 |
| *Sk3* | 30 | 2.0 | 62.6 | 14.4 | 0.012 | $1.90 \times 10^{-3}$ | 1.1749 | 4.6 | 7.6 | 212.5 |
| *Sk4* | 20 | 3.5 | 190.4 | 8.3 | 0.007 | $1.57 \times 10^{-3}$ | 1.2577 | 13.9 | 3.3 | 385.3 |
| *Sk5* | 20 | 3.7 | 297.8 | 11.4 | 0.01 | $9.88 \times 10^{-4}$ | 1.1170 | 11.1 | 3.9 | 287.3 |
| *Sk6* | 20 | 2.8 | 580.9 | 49.8 | 0.047 | $1.88 \times 10^{-3}$ | 1.0601 | 9.8 | 4.3 | 331.8 |
| *Sk7* | 20 | 2.4 | 166.3 | 22.8 | 0.019 | $3.25 \times 10^{-3}$ | 1.1897 | 10.2 | 4.1 | 412.1 |

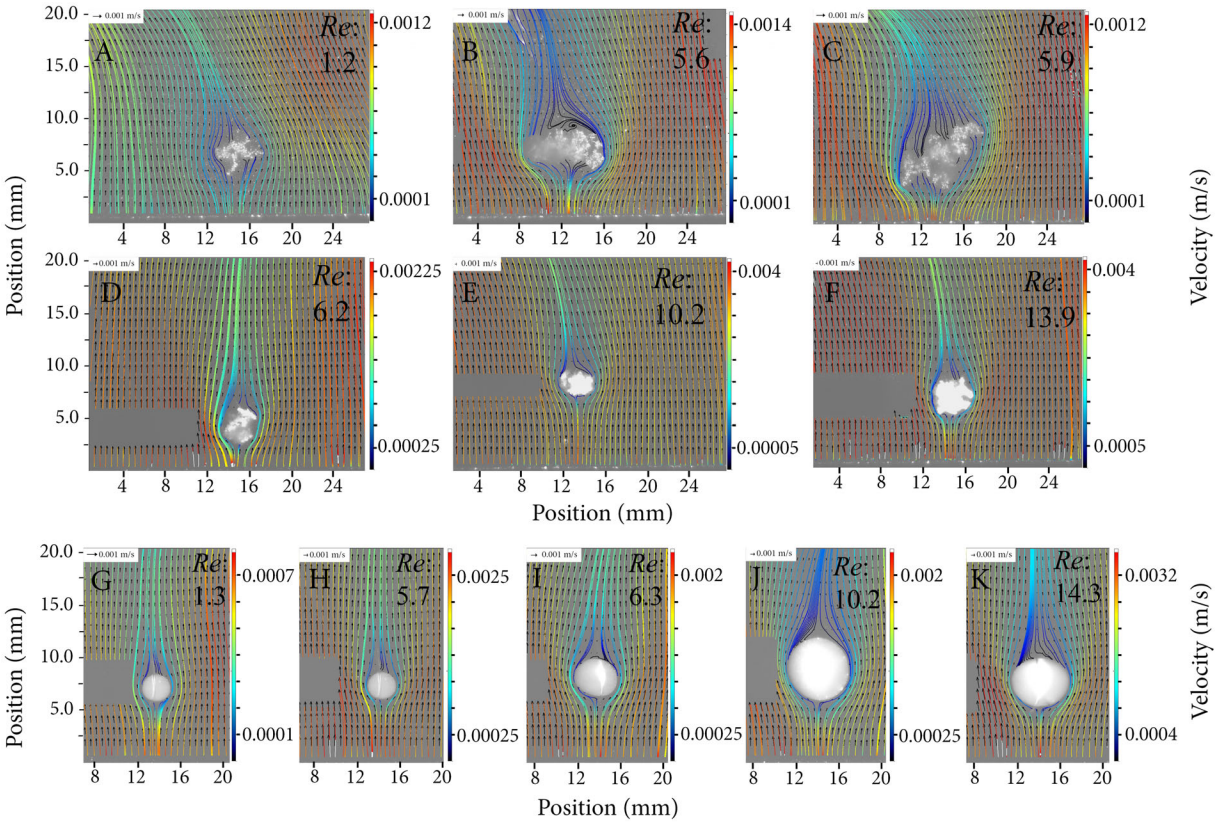


**Fig. 3** Velocity distribution images of different aggregates formed from *Chaetoceros affinis* **(A-C)** or *Skeletonema marinoi* (**D-F**) cells, with different Reynolds (*Re)* numbers. Model aggregates with corresponding *Re* numbers are shown in **G-K**. The gray squares are masked-out areas due to shadowing of the laser sheet. To ensure clarity of the image, only 1/4 of the vectors are displayed in the x-direction and 1/8 in the y-direction.

### Statistical analysis

Differences between aggregate measurements were statistically analyzed using the statistical analysis routines incorporated into SigmaPlot 14.0 (Systat Software Inc., USA) with a significance level of $p < 0.05$. Where assumptions of normality and/or homogeneity of variance failed, nonparametric Mann Whitney U tests were used instead of *t*-tests.

## *Results*

### Aggregate formation

Aggregates of *Chaetoceros* cells formed at the cell concentration of $9 \times 10^6$ cells $L^{-1}$ and were flocculent and porous but stable enough for experimental handling. Generally, they were highly irregular in shape, i.e., nonspherical. At the two higher cell concentrations ($20–30 \times 10^6$ cells $L^{-1}$), however, aggregates were very fragile and consistently fell apart during handling except for two aggregates. In contrast, *Skeletonema* formed aggregates only at these higher cell concentrations ($20–30 \times 10^6$ cells $L^{-1}$). They were compact and near-spherical in shape.

### Aggregate characterization

Aggregate size (ESD) ranged from 2 to 3.7 mm for *Skeletonema*, averaged 2.9 mm, and was significantly smaller than those measured for the *Chaetoceros* aggregates, which ranged from 2.8 to 6.7 mm and averaged 4.8 mm (*t*-test, t = 4.047, df = 14, $p < 0.001$). Generally *Skeletonema* aggregates were more compact and dense as reflected by their higher sinking velocities (range 158–412 m $d^{-1}$) compared to the *Chaetoceros* aggregates (13–124 m $d^{-1}$) (*t*-test, t = –7.264, df = 19, $p < 0.001$) (Fig. 1).

However, no significant difference was observed in their *DW*, with averages of 261 $\mu$g and 282 $\mu$g for *Skeletonema* and *Chaetoceros*, respectively (Mann–Whitney U-test, $p > 0.05$). Consequently, dry weight per aggregate volume was significantly higher in *Skeletonema* compared to *Chaetoceros* (Table 1). Yet, there was a large variability for aggregate dry weight per volume within a species that did not seem to have an influence on the drag coefficient. Aggregates with similar size and drag coefficients within each species could, however, have a very wide range of dry weights per volumes. This variability of dry weight per volume as well as low excess density and sinking velocity may partly be explained by convoluted shape, which includes areas devoid of cells and TEP in the periphery of *Chaetoceros* aggregates. Apparent excess density was an order of magnitude higher in *Skeletonema* aggregates compared to those of *Chaetoceros*, but both solid matter density and cellular volume fraction were relatively similar in

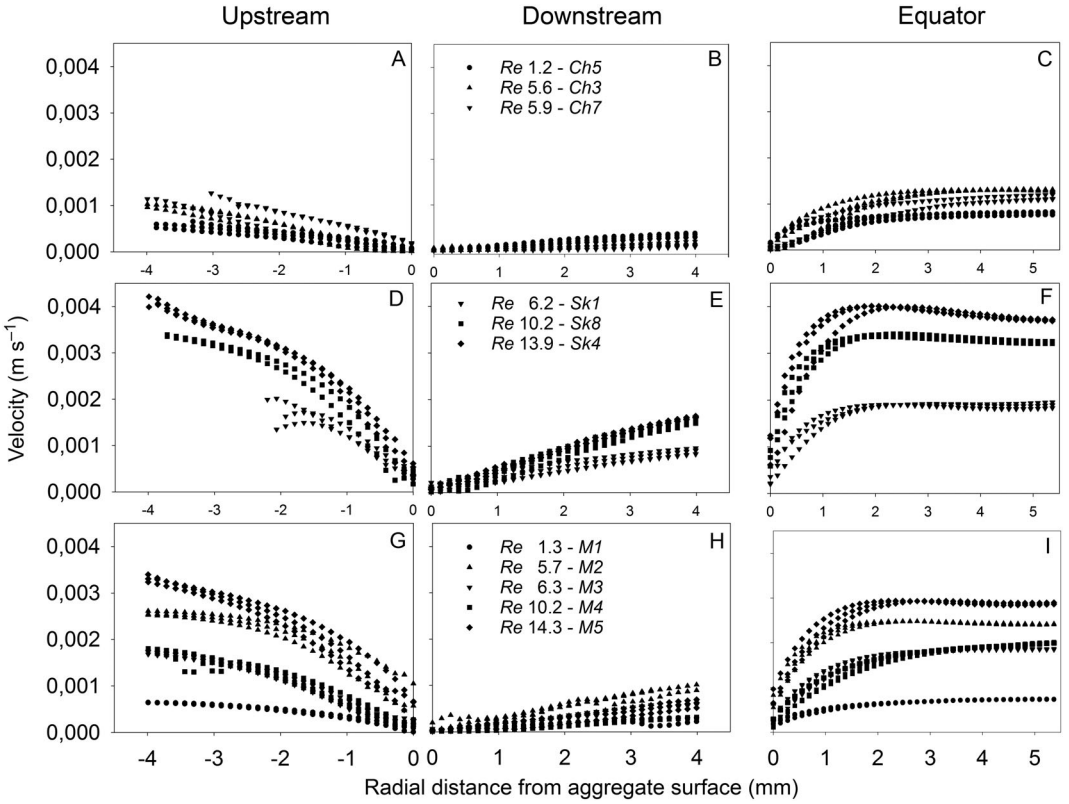


**Fig. 4** Measured velocity profiles up- and down-stream of the aggregate surface and off the aggregates' equators at various Reynolds (*Re)* numbers for three *Chaetoceros affinis* (**A–C**), three *Skeletonema marinoi* aggregates (**D–F**) and five model aggregates (**G–I**). Triplicate profiles around individual aggregates measured in parallel are depicted. Corresponding images of the aggregates are shown in Fig. 3.

*Skeletonema* and *Chaetoceros* (Table 1). Excess density of agar spheres (0.0011 g $cm^{-3}$) has previously been determined in Ploug et al. (2010).

**Particle image velocimetry measurements**

The trajectories of the PIV tracer particles allowed the calculation of the flow fields around the various types of aggregates. The resulting streamlines showed that water was essentially deflected from the aggregate surface, also for highly irregular geometries (Fig. 3). Although streamlines approached the aggregates at almost perpendicular angles upstream of the aggregate surface, no particles were observed to enter the aggregates, that is, passed through them or were scavenged in the aggregate interior. Flow velocities in the downstream wake were substantially slower several diameters away from the surface as compared to those in the upstream region independent of aggregate geometry. After passing around the aggregates, the flow converged toward the centerline in the downstream flow field and further away from the aggregate returned to a simple structure with uniform streamlines parallel to the centerline. No recirculation of flow in the downstream wake was detected for any of the aggregates and *Re* numbers tested. Skewed (either to the left or right) downstream streamlines at low *Re* numbers were an artifact of the flow chamber, which only had a relatively uniform flow field across the upper chamber when mean flow velocities were > 1.0 mm $s^{-1}$ (Ploug and Jørgensen 1999). At higher *Re*, the skewness may have been an artifact of an unevenness of flow leaving the eight outlets of the flow chamber. Uneven background flow was more pronounced for *Chaetoceros* aggregates due to the lower flow rates compared to *Skeletonema* and model aggregates.

Detailed velocity distributions of the equatorial, upstream, and downstream regions of aggregates with irregular geometry formed by *Chaetoceros* cells (Fig. 4A–C) revealed similar distributions to the compact, dense, and generally spherical aggregates formed by *Skeletonema* (Fig. 4D–F). Observed differences between the two species reflected the higher sinking velocities of the *Skeletonema* aggregates.

The approximated shear rates due to velocity gradients around selected model and diatom aggregates with similar sizes and *Re* numbers are visualized in Fig. 5. As expected, the shear rates were highest along the edges of the upstream–downstream axis of the aggregates. Compared to the spherical model aggregates (Fig. 5B, D), the shear rates at the surface of irregularly shaped diatom aggregates (Fig. 5A, C) varied more, and both local maxima with steeper velocity gradients and local minima with less steep gradients were formed. Note that the shear rate was not depicting well the measured velocity gradient at the poles where flow was normal to the aggregate surface and was decelerated or accelerated (compare with

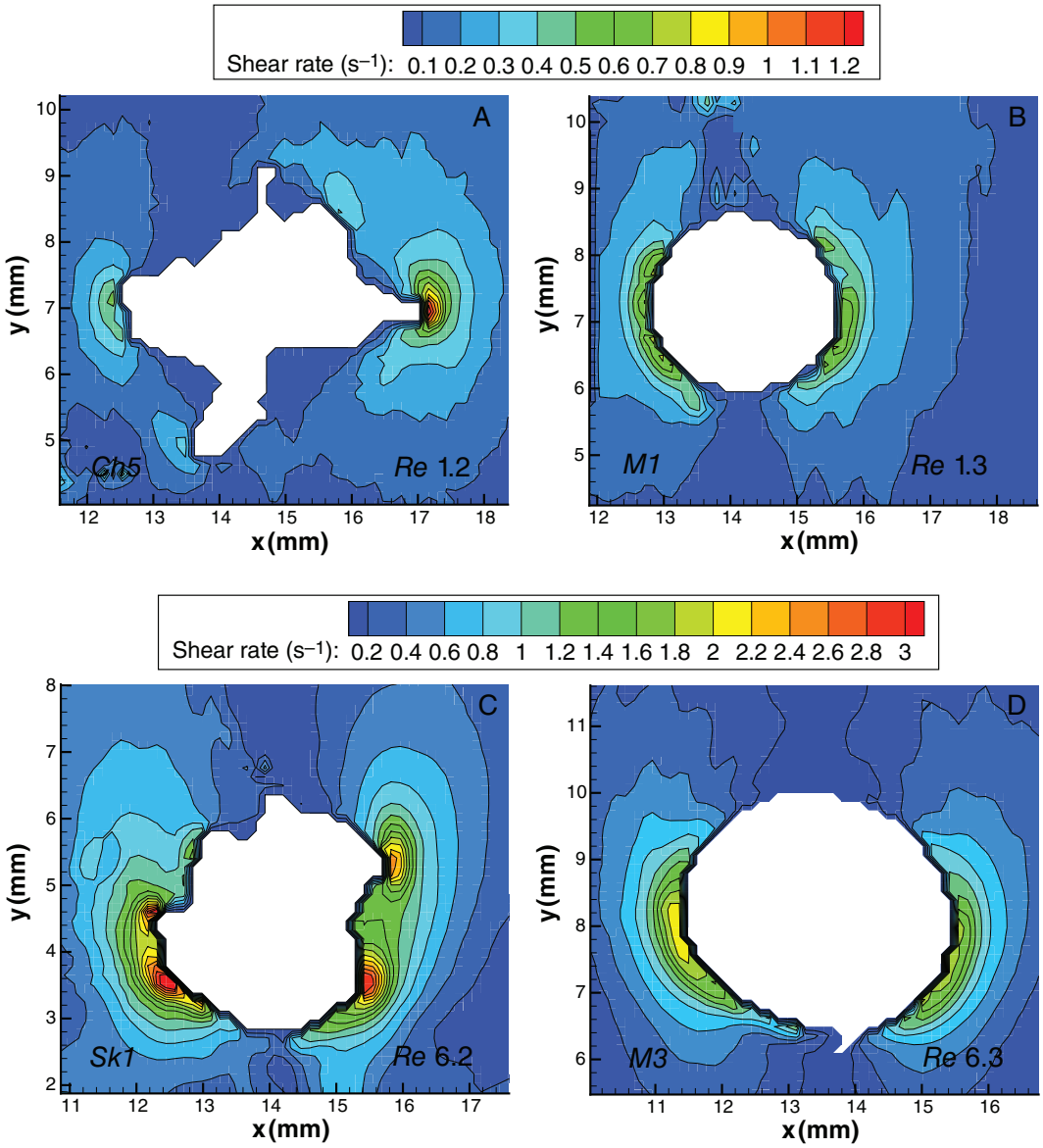


**Fig. 5** Comparison of approximate resultant shear rates around irregular aggregates of diatoms (**A**, **C**) and spherical model aggregates (**B**, **D**) at a Reynolds (*Re*) number of approx. 1 (**A**, **B**) and *Re* of approx. 6 (**C**, **D**). Note different shear rate scales for the different *Re*. Aggregate labels correspond to those used in Figs. 3 and 4.

Figs. 3 and 4). Here, the velocity gradient is determined by the strain rate.

For all aggregates investigated, vorticity was associated with small-scale curvatures along the aggregate surface and its distribution was affected by aggregate shape (Fig. 6). The vorticity in the wake behind the aggregates was low at these relatively low *Re* numbers. At *Re* of approximately 1, the vorticity in the wake behind the irregular *Chaetoceros* aggregate was slightly higher than for the spherical model aggregate (Fig. 6A,B). However, this was only apparent on the right side of the aggregate. At *Re* of approximately 6, there was no obvious difference in wake vorticity between the *Skeletonema* aggregate and the model aggregate (Fig. 6C,D).

### Aggregate imaging

The holographic $D^3HM$ imagery (Fig. 7) and light microscopy (Fig. 8) also confirmed the compact nature of the *Skeletonema* aggregates compared to the smaller volume fraction of cells in *Chaetoceros* aggregates. In the holograms, it is clearly noticeable how tightly aggregated the cells in *Skeletonema* aggregates were since very little light penetrated the main body of the aggregate as shown by the darkened areas from all the cells overlapping each other (Fig. 7A,B). In contrast, *Chaetoceros* aggregates clearly showed interstitial spaces between the cells and were never so densely aggregated in their layers going through the aggregate that the overlap of all the layers completely blocked light passing through the aggregates

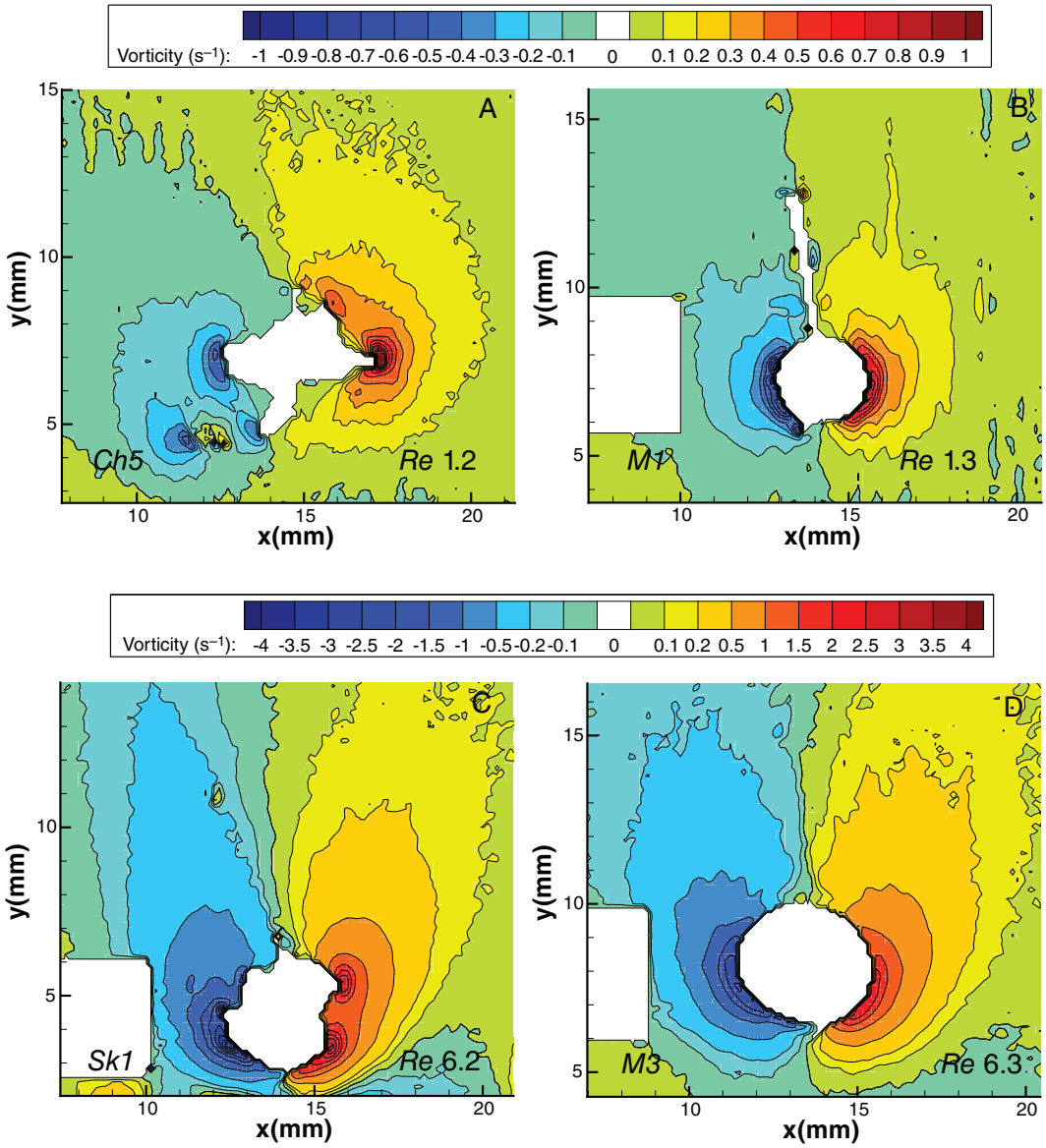


**Fig. 6** Comparison of vorticity around and downstream of irregular aggregates of diatoms (**A**, **C**) and spherical model aggregates (**B**, **D**) at a Reynolds (*Re*) number of approx. 1 (**A**, **B**) and *Re* of approx. 6 (**C**, **D**). Note different vorticity scales for the different *Re* and the unequal isoline width for the bottom diagrams. Aggregates are the same as shown in Fig. 5.

(Fig. 7C,D,E,G). Lower OPL values were also observed in the interstitial spaces compared to the seawater surrounding the aggregates suggesting that a material different from seawater was present in these spaces (Fig. 7F,H). However, the difference in OPL values was very small (< 0.1 $\mu$m) implying that the interstitial substance was of a watery consistency, that is, that the refractive indices of the two substances were very similar.

TEP particles were observed in both *Skeletonema* as well as *Chaetoceros* aggregates, but the staining pattern was distinctly different between the two algal species (Fig. 8). In *Skeletonema* aggregates, staining was predominantly observed around the edges of the aggregates (Fig. 8A,B) with only some minor intrusions into the aggregates themselves, whereas Alcian blue-stained polysaccharide material in *Chaetoceros* aggregates was found as a dominant component within the aggregates' interstitial spaces (Fig. 8C,D). At higher magnifications it became clear that the cell walls and spines of *Chaetoceros* cells were covered by TEP (Fig. 8E,F).

### Oxygen measurements

Oxygen distributions within *Chaetoceros* aggregates were difficult to measure due to their flocculent nature and stickiness. Often the $O_2$ microsensor would stick to the aggregate at some point and hence distort further measurements. An example of the radial oxygen concentrations within both *Skeletonema* and *Chaetoceros* aggregates, respectively, are shown (Fig. 9). The

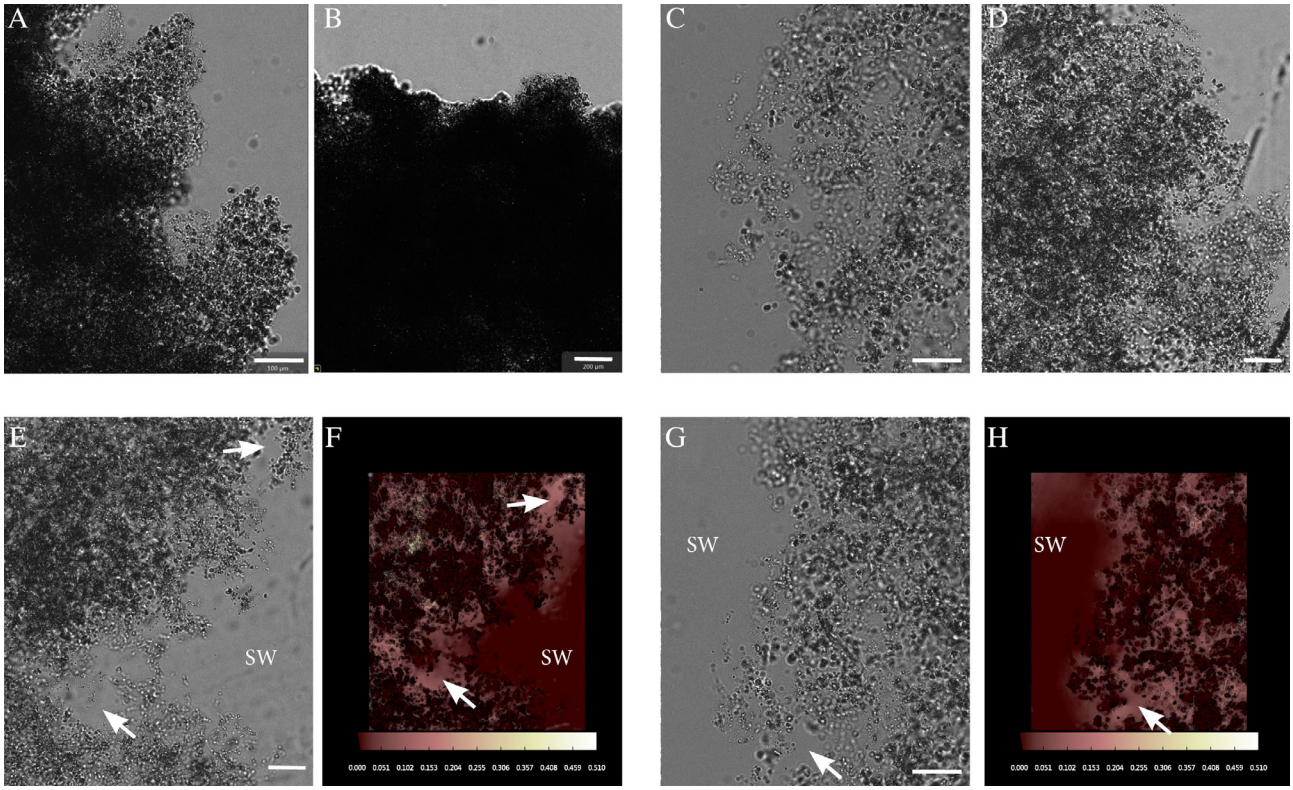


**Fig. 7** Digital holographic microscopy images of diatom aggregates. Extracted intensity images showing the edges of dense compact *Skeletonema marinoi* aggregates (**A**, **B**) compared with *Chaetoceros affinis* aggregates (**C**, **D**) that have numerous interstitial spaces between cells within the aggregates. Intensity images (**E**, **G**) and the respective falsely colored phase images (**F**, **H**) of edges of two different *Chaetoceros* aggregates are shown where interstitial spaces (indicated with arrows) were observed to have different optical heights than the surrounding seawater (SW), suggesting the presence of transparent exopolymeric particles (TEP). The color scheme for the phase images was chosen to clearly depict differences in optical height. Shown scale bars are 200 $\mu$m for images **B**, **D**, **E** and 100 $\mu$m for **A**, **C**, **G**.

oxygen concentration distributions within aggregates relative to that in the ambient water within the aggregates were similar to those modeled for suspended aggregates impermeable to flow and those measured and modeled in similar aggregates previously (Ploug 2001; Moradi et al. 2018). However, the measured oxygen concentrations and gradients in the wake downstream of the sinking aggregates were lower than those modeled without flow in both the downstream and in the upstream region, and reflect that advective transport was more important than diffusion outside the aggregates. These deviations were higher for the *Skeletonema* aggregate with a sinking velocity of 287 m $d^{-1}$, as compared to the *Chaetoceros* aggregate with a sinking velocity of 25.5 m $d^{-1}$. The *Skeletonema* aggregate was 3.7 mm (ESD) large while the *Chaetoceros* aggregate was 4.5 mm (ESD) large. The lower $O_2$ concentrations within *Skeletonema* aggregates demonstrate a higher respiration rate per aggregate volume relative to that of the *Chaetoceros* aggregate.

## Discussion

The scavenging of small particles and the uptake or release of gases, nutrients, and solutes by fast-sinking marine snow are important in regulating the $CO_2$ concentration in the earth's atmosphere. Models and experimental studies of flow distributions around sinking particles and aggregates, such as diatom aggregates, have to date focused on spherical geometry (Kiørboe et al. 2001; Moradi et al. 2018). Aggregates in the field, however, are seldom spherical. Using PIV, we obtained high-resolution flow distributions for diatom aggregates with various geometries and uneven surfaces as well as spherical model aggregates. In combination with holographic imaging, $O_2$ microsensors and modeling, we investigated the impact of aggregate composition on flow and diffusion within and around aggregates.

Two different types of diatom aggregates were studied: (1) nearly spherical and compact aggregates formed by *Skeletonema* cell chains, and (2) predominantly nonspherical and more flocculent aggregates formed by *Chaetoceros* cell chains, and further compared to almost perfectly spherical nonpermeable model aggregates. *Skeletonema* formed aggregates only at higher cell concentrations relative to *Chaetoceros*. This was most likely due to the presence of *Chaetoceros'* entanglement-enhancing spines (Alldredge and Gotschalk 1989) and its high TEP production, which was also observed

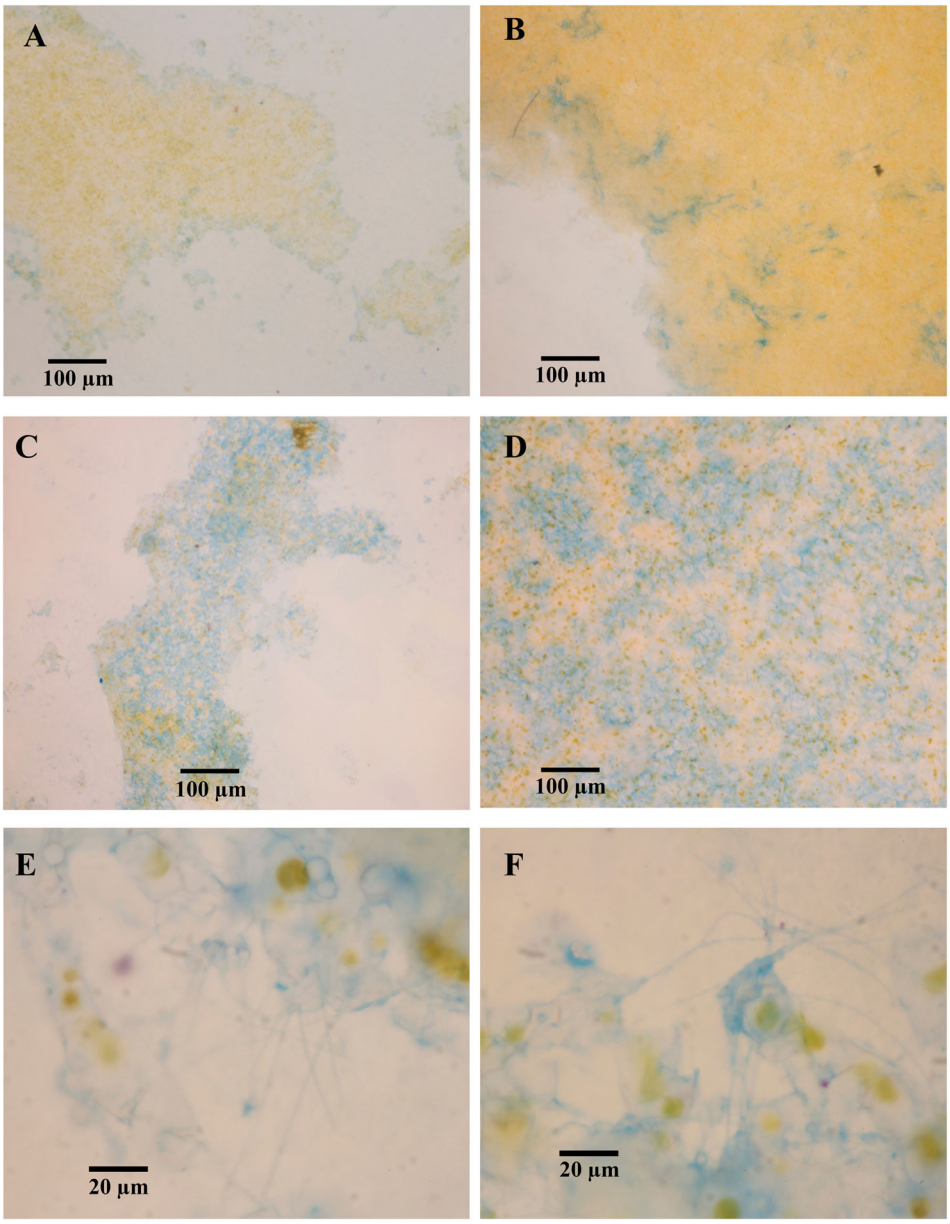


**Fig. 8** (**A**, **B**) Aggregates formed by *Skeletonema marinoi* cells showed Alcian blue staining and thus the presence of transparent exopolymeric particles (TEP) predominantly on the edges of aggregates. In contrast, TEP formed a dominant component of the interstitial spaces in aggregates formed by *Chaetoceros affinis* (**C**, **D**). Particularly, the spines and cell walls of *C. affinis* showed Alcian blue staining (**E**, **F**). (**A**–**D**): 4× objective, (**E**, **F**) 100× oil objective.

on the spines (Kiørboe and Hansen 1993; Crocker and Passow 1995). *Chaetoceros* aggregates were fluffy in appearance, never similar in shape, and frequently revealed various protrusions (Fig. 2A–C). It has previously been shown that *Chaetoceros* coagulation depends on TEP-TEP or TEP-cell stickiness (Kiørboe and Hansen 1993; Passow et al. 1994; Logan et al. 1995) while that for *Skeletonema* depends on cell–cell stickiness (Kiørboe and Hansen 1993; Ziervogel and Forster 2005). With the Alcian blue staining we observed a general lack of TEP within *Skeletonema* aggregates, but it was highly present within *Chaetoceros* aggregates (Fig. 8). Here, TEP was present between the cell chains as well as around individual cells along the cell walls and spines (Fig. 8). TEP is sticky (Alldredge et al. 1993; Passow 2002; Mari et al. 2017) and thus creates a matrix of cell chains and spines that are glued together. The presence of low density TEP in *Chaetoceros* aggregates most likely also decreased the size-specific sinking velocities of *Chaetoceros* aggregates (13–124 m $d^{-1}$) compared to the fast-sinking, dense *Skeletonema* aggregates (range 158–412 m $d^{-1}$) (Engel and Schartau 1999) as some recent studies have

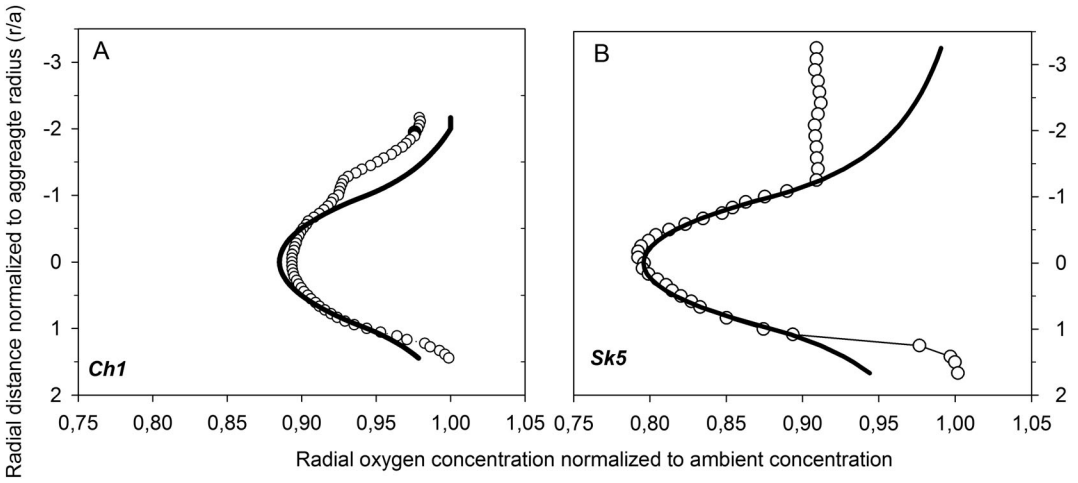


**Fig. 9** Examples of the radial oxygen distribution relative to the concentration in the ambient water of a *Chaetoceros affinis* (**A**) and a *Skeletonema marinoi* (**B**) aggregate. Radial distance from the aggregate center was normalized to aggregate radius (A). Open symbols represent measured values, and the black curve the modeled values for suspended, nonsinking aggregates impermeable to flow. Corresponding aggregate characteristics are found in Table 1.

demonstrated positive buoyancy of TEP (Azetsu-Scott and Passow 2004; Mari et al. 2017).

Overall, all measured sinking velocities were within the expected range for marine snow (Alldredge and Gotschalk 1988); however, the sinking velocity of larger *Chaetoceros* aggregates was slower than for smaller *Skeletonema* aggregates, and there was no relationship between the dry weight of the aggregates and their sinking velocity (linear regression, $r = 0.03$) confirming observations by Alldredge and Gotschalk (1988). Aggregate dry weight per volume was higher in *Skeletonema* as compared to that of *Chaetoceros* aggregates but the large variability within a diatom species prevents any clear relationships with the drag coefficient and ultimately sinking velocity. We expect that shape may also affect the observed differences in sinking velocity. Drag and therefore settling velocity of an aggregate are functions of its shape (Komar and Reimers 1978), and nonspherical aggregates are expected to sink slower than spherical ones (Simpson 1982; Alldredge and Gotschalk 1988). Our limited observations within one species do not allow for such conclusions. However, the nonspherical *Chaetoceros* indeed showed slower sinking velocities and lower apparent excess densities as compared to those of the nearly spherical *Skeletonema* aggregates.

We are not aware of other studies that have investigated irregularly shaped diatom aggregates with PIV to provide high spatial resolution of the flow field around the aggregates as a function of *Re*. Viscous forces dominate water movement at $Re < 0.1$, while inertial forces dominate at higher *Re*. As demonstrated in the present study and earlier, streamlines change from being symmetrical upstream and downstream of a sinking aggregate at $Re < 0.1$ (i.e., Stokes "creeping" flow) to become increasingly asymmetrical at higher *Re* (Kiørboe et al. 2001). PIV clearly depicted the curvilinear feature of the streamlines in a wake with retarded fluid flow downstream in all aggregate types similar to those modeled in previous studies with spherical geometries (Kiørboe et al. 2001; Moradi et al. 2018). In our study we observed very similar flow around both types of diatom aggregates as well as the model spheres at a millimeter scale. Vorticity measured around spherical aggregates was similar to that predicted by theory and previously modeled by Kiørboe et al. (2001). At $Re \sim 1$, the trail of vorticity downstream of a sinking, highly irregularly shaped diatom aggregate tends to extend further than for a spherical model aggregate (Fig. 6A,B). At $Re \sim 6$, however, there was no obvious difference to the downstream vorticity field of the nearly spherical diatom aggregate compared to that of the spherical model (agar) aggregate (Fig. 6C,D). The streamline images (Fig. 3) demonstrated that no flow separation occurred in the wake behind aggregates (i.e., downstream) at these *Re*.

Whereas velocity gradients along the surface of spherical model aggregates smoothly change along the upstream–downstream axis as predicted by theory (Kiørboe et al. 2001), the velocity gradients varied more along the surface of irregularly shaped diatom aggregates. Irregular surfaces of sinking diatom aggregates produced local maxima and minima of shear rates and vorticity relative to the smoother variation around sinking spheres (Figs. 5, 6). High shear rates imply steep velocity gradients in flow tangential to the surface. Encounter and thus potential coagulation with particles and colonization by bacteria from the ambient water are highest where the velocity gradients are steepest. Thus local growth of the aggregates via scavenging is expectedly highest in these regions.

Diatom aggregates are fractal and the cellular volume fraction decreases significantly with increasing aggregate size (Alldredge and Gotschalk 1988). Model calculations have

indicated that fluid flow in the order of 26 to 160 $\mu$m $s^{-1}$ may occur in large (7–20 mm diameter), sinking diatom aggregates with cellular volume fractions <0.0001 (Logan and Alldredge 1989). However, that model did not include TEP to be part of the aggregate matrix as TEP was only discovered a few years later (Alldredge et al. 1993). The aggregates in our study were all smaller and had more than 10-fold higher volume fractions of cells as compared to the aggregates studied by Logan and Alldredge (1989). In our study, the $O_2$ distributions within both *Skeletonema* and *Chaetoceros* aggregates were similar to those previously reported for these types of diatom aggregates and similar to those of spheres and other aggregates impermeable to flow (Ploug et al. 1997; Ploug et al. 1999*b*; Ploug and Bergkvist 2015; Moradi et al. 2018). The $O_2$ concentrations within *Skeletonema* aggregates normalized to size were lower than those in *Chaetoceros*, and imply that the $O_2$ consumption per volume aggregates was higher in the compact *Skeletonema* aggregates with more dry weight (cells) per volume as compared to those formed by *Chaetoceros*. These observations suggest that the interstitial spaces observed in *Chaetoceros* cells were indeed largely filled with TEP. What appears as empty space by eye, in fact, is a matrix of cells and TEP. Digital holographic microscopy has the ability to detect certain polymeric substances (Zetsche et al. 2016*a*; Zetsche et al. 2016*b*), and the imaging of *Chaetoceros* aggregates suggests that a substance different in its optical properties was present in the interstitial spaces compared with the surrounding seawater (Fig. 7). The OPL differences were very small, yet support what is known for TEP: It has very similar properties to stagnant water (Ploug and Passow 2007), which unfortunately also does not facilitate a stronger optical signal in the observed holograms.

Clogging of pores in aggregates by extracellular polymeric substances (EPS) has been observed in microbial aggregates such as sludge flocs and granules (Li and Yuan 2002; Sheng et al. 2010) decreasing the mass transfer efficiency of substrates. The direct impact of TEP (a particulate form of EPS) filling up pore spaces on mass transfer in diatom aggregates was previously studied using a diffusivity microsensor (Ploug and Passow 2007). That study showed that the apparent diffusivity of gases in diatom aggregates with TEP is close to that of stagnant water. Observed $O_2$ profiles in other studies and here also indicate that the apparent diffusion coefficient of $O_2$ in aggregates is close to that in stagnant water (Ploug et al. 2008). The wake with $O_2$-depleted water in the downstream region is due to respiration within aggregates and a consequence of the retarded flow in the wake of the aggregate as measured and modeled earlier (Kiørboe et al. 2001; Ploug 2001; Moradi et al. 2018).

A wake with concentration gradients of nutrients and solutes leaking from sinking aggregates was hypothesized almost two decades ago as a consequence of high hydrolytic activities by aggregate-attached bacteria (Smith et al. 1992; Azam and Long 2001). Almost at the same time, the wake behind sinking aggregates impermeable to flow was demonstrated for aggregates with *Re* numbers between 1 and 10 (Kiørboe et al. 2001; Ploug 2001). Since then, experimental studies and models have shown that bacterial chemotaxis helps bacteria to locate and colonize the wake behind sinking aggregates (Stocker et al. 2008), and even zooplankton localize and find aggregates due to the long wake with retarded fluid motion and concentration gradients of solutes (Jackson and Kiørboe 2004; Lombard et al. 2013). Hence, the wake behind sinking aggregates as demonstrated here and in other studies appears to be crucial for both bacteria and zooplankton during their degradation of sinking aggregates. Most studies have focused on chemotaxis as the key foraging mechanism for bacteria and zooplankton to locate sinking aggregates. The composition of leaking chemical compounds in the wake of aggregates, however, may largely vary across different aggregate sources and also change during degradation. Our study demonstrates the retarded flow in the wake. This physical signature by a sinking aggregate in the water is expectedly more stable during microbial aggregate degradation and suggests rheotaxis as an alternative strategy used by foraging zooplankton.

In conclusion, overall similar flow distributions at a millimeter scale were evident around both spherical aggregates and irregularly shaped aggregates. However, the irregular shape caused heterogeneity of velocity gradients and vorticity distributions on a micrometer scale along the aggregate surface with local minima and maxima as compared to those along spherical model aggregates. *Chaetoceros* chains formed nonspherical porous aggregates, most likely due to their TEP-coated spines, but also featured a strong presence of TEP within their interstitial spaces which most likely caused aggregates to behave in a similar way to the less permeable and more spherical *Skeletonema* aggregates. To our knowledge, fluid flow has never been empirically demonstrated with in diatom aggregates. Theoretical models of interstitial flow through diatom aggregates were adapted to models developed from observations in model aggregates composed of steel threads before TEP was discovered (Adler 1981; Logan and Alldredge 1989). Therefore, its applicability as a model for fragile diatom aggregates is, in fact, questionable. Our study demonstrates that while diffusion can be the major mechanism of mass transfer within aggregates, aggregate topography is significant for local variability in small-scale velocity gradients along the surface potentially enhancing both coagulation with other particles as well as colonization by microbiota as compared to ideally spherical aggregates with a smooth surface.

## References

Adler, P. M. 1981. Streamlines in and around porous particles. J. Colloid Interface Sci. **81**: 531–535. https://doi.org/10.1016/0021-9797(81)90434-3

Alldredge, A. L., and C. Gotschalk. 1988. In situ settling behavior of marine snow. Limnol. Oceanogr. **33**: 339–351. doi:10.4319/lo.1988.33.3.0339

Alldredge, A. L., and C. C. Gotschalk. 1989. Direct observations of the mass flocculation of diatom blooms: Characteristics, settling velocities and formation of diatom aggregates. Deep-Sea Res. Pt. A **36**: 159–171. doi:10.1016/0198-0149(89)90131-3

Alldredge, A. L., U. Passow, and B. E. Logan. 1993. The abundance and significance of a class of large, transparent organic particles in the ocean. Deep-Sea Res. Pt. I **40**: 1131–1140. doi:10.1016/0967-0637(93)90129-q

Azam, F., and R. A. Long. 2001. Sea snow microcosms. Nature **414**: 495. doi:10.1038/35107174

Azetsu-Scott, K., and U. Passow. 2004. Ascending marine particles: Significance of transparent exopolymer particles (TEP) in the upper ocean. Limnol. Oceanogr. **49**: 741–748. doi:10.4319/lo.2004.49.3.0741

Bergkvist, J., I. Klawonn, M. J. Whitehouse, G. Lavik, V. Brüchert, and H. Ploug. 2018. Turbulence simultaneously stimulates small-and large-scale $CO_2$ sequestration by chain-forming diatoms in the sea. Nat. Commun. **9**: 3046. doi:10.1038/s41467-018-05149-w

Bižić-Ionescu, M., D. Ionescu, and H.-P. Grossart. 2018. Organic particles: Heterogeneous hubs for microbial interactions in aquatic ecosystems. Front. Microbiol. **9**: 2569. doi:10.3389/fmicb.2018.02569

Broecker, W. S., and T.-H. Peng. 1974. Gas exchange rates between air and sea. Tellus **26**: 21–35. doi:10.3402/tellusa.v26i1-2.9733

Burd, A. B., and G. A. Jackson. 2009. Particle aggregation. Ann. Rev. Mar. Sci. **1**: 65–90. doi:10.1146/annurev.marine.010908.163904

Crocker, K. M., and U. Passow. 1995. Differential aggregation of diatoms. Mar. Ecol. Prog. Ser. **117**: 249–257. doi:10.3354/meps117249

Cronenberg, C. C. H. 1994. Biochemical engineering on a microscale: Biofilms investigated with needle-type glucose sensors. PhD. Van 't Hoff Institute for Molecular Sciences (HIMS). University of Amsterdam, The Netherlands.

Delong, E. F., D. G. Franks, and A. L. Alldredge. 1993. Phylogenetic diversity of aggregate-attached vs. free-living marine bacterial assemblages. Limnol. Oceanogr. **38**: 924–934. doi:10.4319/lo.1993.38.5.0924

Engel, A. 2009. Determination of marine gel particles, p. 125–142. *In* O. Wurl [ed.], Practical guidelines for the analysis of seawater. CRC Press.

Engel, A., and M. Schartau. 1999. Influence of transparent exopolymer particles (TEP) on sinking velocity of *Nitzschia closterium* aggregates. Mar. Ecol. Prog. Ser. **182**: 69–76. doi:10.3354/meps182069

Grossart, H.-P., and H. Ploug. 2001. Microbial degradation of organic carbon and nitrogen on diatom aggregates. Limnol. Oceanogr. **46**: 267–277. doi:10.4319/lo.2001.46.2.0267

Grossart, H.-P., K. W. Tang, T. Kiørboe, and H. Ploug. 2007. Comparison of cell-specific activity between free-living and attached bacteria using isolates and natural assemblages. FEMS Microbiol. Lett. **266**: 194–200. doi:10.1111/j.1574-6968.2006.00520.x

Guillard, R. R. L. 1975. Culture of phytoplankton for feeding marine invertebrates, p. 29–60. *In* Culture of marine invertebrate animals. Springer. Boston, MA. doi:10.1007/978-1-4615-8714-9_3

Iversen, M. H., and H. Ploug. 2010. Ballast minerals and the sinking carbon flux in the ocean: Carbon-specific respiration rates and sinking velocity of marine snow aggregates. Biogeosciences **7**: 2613–2624. doi:10.5194/bg-7-2613-2010

Jackson, G. A., and T. Kiørboe. 2004. Zooplankton use of chemodetection to find and eat particles. Mar. Ecol. Prog. Ser. **269**: 153–162. doi:10.3354/meps269153

Kiørboe, T., and J. L. S. Hansen. 1993. Phytoplankton aggregate formation: Observations of patterns and mechanisms of cell sticking and the significance of exopolymeric material. J. Plankton Res. **15**: 993–1018. doi:10.1093/plankt/15.9.993

Kiørboe, T., H. Ploug, and U. H. Thygesen. 2001. Fluid motion and solute distribution around sinking aggregates I: Small-scale fluxes and heterogeneity of nutrients in the pelagic environment. Mar. Ecol. Prog. Ser. **211**: 1–13. doi:10.3354/meps211001

Komar, P. D., and C. Reimers. 1978. Grain shape effects on settling rates. J. Geol. **86**: 193–209. doi:10.1086/649674

Li, X.-Y., and Y. Yuan. 2002. Collision frequencies of microbial aggregates with small particles by differential sedimentation. Environ. Sci. Technol. **36**: 387–393. doi:10.1021/es010681d

Logan, B. E., and A. L. Alldredge. 1989. Potential for increased nutrient uptake by flocculating diatoms. Mar. Biol. **101**: 443–450. doi:10.1007/bf00541645

Logan, B. E., H.-P. Grossart, and M. Simon. 1994. Direct observation of phytoplankton, TEP and aggregates on polycarbonate filters using brightfield microscopy. J. Plankton Res. **16**: 1811–1815. doi:10.1093/plankt/16.12.1811

Logan, B. E., U. Passow, A. L. Alldredge, H.-P. Grossartt, and M. Simont. 1995. Rapid formation and sedimentation of large aggregates is predictable from coagulation rates (half-lives) of transparent exopolymer particles (TEP). Deep-Sea Res. Pt. II **42**: 203–214. doi:10.1016/0967-0645(95)00012-F

Lombard, F., M. Koski, and T. Kiørboe. 2013. Copepods use chemical trails to find sinking marine snow aggregates. Limnol. Oceanogr. **58**: 185–192. doi:10.4319/lo.2013.58.1.0185

Mari, X., U. Passow, C. Migon, A. B. Burd, and L. Legendre. 2017. Transparent exopolymer particles: Effects on carbon cycling in the ocean. Prog. Oceanogr. **151**: 13–37. doi:10.1016/j.pocean.2016.11.002

Moeseneder, M. M., C. Winter, and G. J. Herndl. 2001. Horizontal and vertical complexity of attached and free-living bacteria of the eastern Mediterranean Sea, determined by 16S rDNA and 16S rRNA fingerprints. Limnol. Oceanogr. **46**: 95–107. doi:10.4319/lo.2001.46.1.0095

Moradi, N., B. Liu, M. Iversen, M. M. Kuypers, H. Ploug, and A. Khalili. 2018. A new mathematical model to explore microbial processes and their constraints in phytoplankton colonies and sinking marine aggregates. Sci. Adv. **4**: eaat1991. doi:10.1126/sciadv.aat1991

Narayanan, J., J.-Y. Xiong, and X.-Y. Liu. 2006. Determination of agarose gel pore size: Absorbance measurements vis a vis other techniques, J. Phys.: Conference Series. **28**: 83–86. doi:10.1088/1742-6596/28/1/017

Nelson, D. M., P. Tréguer, M. A. Brzezinski, A. Leynaert, and B. Quéguiner. 1995. Production and dissolution of biogenic silica in the ocean: Revised global estimates, comparison with regional data and relationship to biogenic sedimentation. Global Biogeochem. Cycles **9**: 359–372. doi:10.1029/95GB01070

Passow, U. 2002. Transparent exopolymer particles (TEP) in aquatic environments. Prog. Oceanogr. **55**: 287–333. doi:10.1016/s0079-6611(02)00138-6

Passow, U., A. L. Alldredge, and B. E. Logan. 1994. The role of particulate carbohydrate exudates in the flocculation of diatom blooms. Deep-Sea Res. Pt. I **41**: 335–357. doi:10.1016/0967-0637(94)90007-8

Ploug, H. 2001. Small-scale oxygen fluxes and remineralization in sinking aggregates. Limnol. Oceanogr. **46**: 1624–1631. doi:10.4319/lo.2001.46.7.1624

Ploug, H., and J. Bergkvist. 2015. Oxygen diffusion limitation and ammonium production within sinking diatom aggregates under hypoxic and anoxic conditions. Mar. Chem. **176**: 142–149. doi:10.1016/j.marchem.2015.08.012

Ploug, H., H.-P. Grossart, F. Azam, and B. B. Jørgensen. 1999*a*. Photosynthesis, respiration, and carbon turnover in sinking marine snow from surface waters of Southern California bight: Implications for the carbon cycle in the ocean. Mar. Ecol. Prog. Ser. **179**: 1–11. doi:10.3354/meps179001

Ploug, H., S. Hietanen, and J. Kuparinen. 2002. Diffusion and advection within and around sinking, porous diatom aggregates. Limnol. Oceanogr. **47**: 1129–1136. doi:10.4319/lo.2002.47.4.1129

Ploug, H., M. H. Iversen, and G. Fischer. 2008. Ballast, sinking velocity, and apparent diffusivity within marine snow and zooplankton fecal pellets: Implications for substrate turnover by attached bacteria. Limnol. Oceanogr. **53**: 1878–1886. doi:10.4319/lo.2008.53.5.1878

Ploug, H., and B. B. Jørgensen. 1999. A net-jet flow system for mass transfer and microsensor studies of sinking aggregates. Mar. Ecol. Prog. Ser. **176**: 279–290. doi:10.3354/meps176279

Ploug, H., M. Kühl, B. Buchholz, and B. Jørgensen. 1997. Anoxic aggregates an ephemeral phenomenon in the ocean. Aquat. Microb. Ecol. **13**: 285–294. doi:10.3354/ame013285

Ploug, H., and U. Passow. 2007. Direct measurement of diffusivity within diatom aggregates containing transparent exopolymer particles. Limnol. Oceanogr. **52**: 1–6. doi:10.4319/lo.2007.52.1.0001

Ploug, H., W. Stolte, and B. B. Jørgensen. 1999*b*. Diffusive boundary layers of the colony-forming plankton alga, *Phaeocystis* sp.-implications for nutrient uptake and cellular growth. Limnol. Oceanogr. **44**: 1959–1967. doi:10.4319/lo.1999.44.8.1959

Ploug, H., A. Terbrüggen, A. Kaufmann, D. Wolf-Gladrow, and U. Passow. 2010. A novel method to measure particle sinking velocity in vitro, and its comparison to three other in vitro methods. Limnol. Oceanogr. Methods **8**: 386–393. doi:10.4319/lom.2010.8.386

Revsbech, N. P. 1989. An oxygen microsensor with a guard cathode. Limnol. Oceanogr. **34**: 474–478. doi:10.4319/lo.1989.34.2.0474

Sanders, R. J., et al. 2016. Controls over ocean mesopelagic interior carbon storage (COMICS): Fieldwork, synthesis, and modeling efforts. Front. Mar. Sci. **3**: 1–10. doi:10.3389/fmars.2016.00136

Shanks, A. L., and E. W. Edmondson. 1989. Laboratory-made artificial marine snow: A biological model of the real thing. Mar. Biol. **101**: 463–470. doi:10.1007/bf00541648

Sheng, G.-P., H.-Q. Yu, and X.-Y. Li. 2010. Extracellular polymeric substances (EPS) of microbial aggregates in biological wastewater treatment systems: A review. Biotechnol. Adv. **28**: 882–894. doi:10.1016/j.biotechadv.2010.08.001

Siegel, D. A., et al. 2016. Prediction of the export and fate of Global Ocean net primary production: The EXPORTS science plan. Front. Mar. Sci. **3**: 1–10. doi:10.3389/fmars.2016.00022

Simon, M., H.-P. Grossart, B. Schweitzer, and H. Ploug. 2002. Microbial ecology of organic aggregates in aquatic ecosystems. Aquat. Microb. Ecol. **28**: 175–211. doi:10.3354/ame028175

Simpson, W. 1982. Particulate matter in the oceans-sampling methods, concentration, size distribution and particle dynamics. Oceanogr. Mar. Biol. **20**: 119–172.

Smith, D. C., M. Simon, A. L. Alldredge, and F. Azam. 1992. Intense hydrolytic enzyme activity on marine aggregates and implications for rapid particle dissolution. Nature **359**: 139–142. doi:10.1038/359139a0

Stief, P., A. Kamp, B. Thamdrup, and R. N. Glud. 2016. Anaerobic nitrogen turnover by sinking diatom aggregates at varying ambient oxygen levels. Front. Microbiol. **7**: 98. doi:10.3389/fmicb.2016.00098

Stocker, R., J. R. Seymour, A. Samadani, D. E. Hunt, and M. F. Polz. 2008. Rapid chemotactic response enables marine bacteria to exploit ephemeral microscale nutrient patches. PNAS **105**: 4209–4214. doi:10.1073/pnas.0709765105

Thiele, S., B. M. Fuchs, R. Amann, and M. H. Iversen. 2015. Colonization in the photic zone and subsequent changes during sinking determine bacterial community composition in marine snow. Appl. Environ. Microbiol. **81**: 1463–1471. doi:10.1128/aem.02570-14

Turner, J. T. 2015. Zooplankton fecal pellets, marine snow, phytodetritus and the ocean's biological pump. Prog.

Oceanogr. **130**: 205–248. doi:10.1016/j.pocean.2014.08.005

White, F. M. 2006. Viscous fluid flow, 3rd ed. McGraw-Hill. doi:10.1109/IEMBS.2006.259657

Volk, T., and M. I. Hoffert. 1985. Ocean carbon pumps: Analysis of relative strengths and efficiencies in ocean-driven atmospheric $CO_2$ changes, p. 99–110. *In* E. T. Sundquist and W. S. Broecker [eds.], The carbon cycle and atmospheric $CO_2$: Natural variations archean to present. American Geophysical Union. doi:10.1029/GM032p0099

Zetsche, E.-M., T. Baussant, F. J. R. Meysman, and D. Van Oevelen. 2016*a*. Direct visualization of mucus production by the cold-water coral *Lophelia pertusa* with digital holographic microscopy. PLoS ONE **11**: e0146766. doi:10.1371/journal.pone.0146766

Zetsche, E.-M., A. El Mallahi, and F. J. R. Meysman. 2016*b*. Digital holographic microscopy: A novel tool to study the morphology, physiology and ecology of diatoms. Diatom Res. **31**: 1–16. doi:10.1080/0269249X.2016.1140679

Zetsche, E., A. El Mallahi, F. Dubois, C. Yourassowsky, J. Kromkamp, and F. J. R. Meysman. 2014. Imaging-in-flow: Digital holographic microscopy as a novel tool to detect and classify nanoplanktonic organisms. Limnol. Oceanogr. Methods **12**: 757–775. doi:10.4319/lom.2014.12.757

Ziervogel, K., and S. Forster. 2005. Aggregation and sinking behaviour of resuspended fluffy layer material. Cont. Shelf Res. **25**: 1853–1863. doi:10.1016/j.csr.2005.06.008

## Acknowledgments

We thank Dr. Johanna Bergkvist for preparing cultures. This study was supported by the University of Gothenburg, and the Swedish Research Councils (VR, Dnr: 2015-05322 to HP and FORMAS, Dnr: 2012-1134 to AIL), as well as an ASSEMBLE grant (227799 to EZ) and Maria Skłodowska Curie Action (project no. MSCA_ IF_GA_660481 to EZ).

## Conflict of Interest

None declared.

*Submitted 14 May 2019*
*Revised 11 November 2019*
*Accepted 08 January 2020*

*Associate editor: Thomas Kiørboe*